Faraday Discussions

Accepted Manuscript

This manuscript will be presented and discussed at a forthcoming Faraday Discussion meeting. All delegates can contribute to the discussion which will be included in the final volume.

Register now to attend! Full details of all upcoming meetings: http://rsc.li/fd-upcoming-meetings

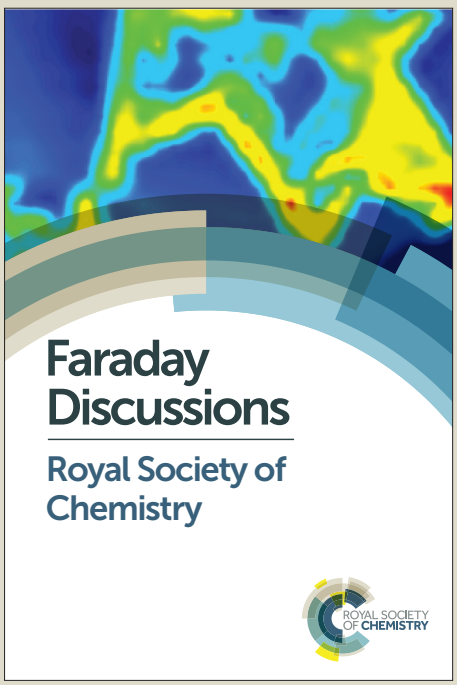

This is an *Accepted Manuscript*, which has been through the Royal Society of Chemistry peer review process and has been accepted for publication.

Accepted Manuscripts are published online shortly after acceptance, before technical editing, formatting and proof reading. Using this free service, authors can make their results available to the community, in citable form, before we publish the edited article. We will replace this *Accepted Manuscript* with the edited and formatted *Advance Article* as soon as it is available.

You can find more information about *Accepted Manuscripts* in the Information for Authors.

Please note that technical editing may introduce minor changes to the text and/or graphics, which may alter content. The journal's standard Terms & Conditions and the Ethical guidelines still apply. In no event shall the Royal Society of Chemistry be held responsible for any errors or omissions in this *Accepted Manuscript* or any consequences arising from the use of any information it contains.

ROYAL SOCIETY OF CHEMISTRY

www.rsc.org/faraday_d

Journal Name

ARTICLE TYPE

Cite this: DOI: 10.1039/xxxxxxxxxx

Near-field Raman Spectroscopy of Nanocarbon Materials

Zachary J. Lapin,[a] Ryan Beams,[b] Luiz Gustavo Cançado,[c] and Lukas Novotny [a]‡

Received Date
Accepted Date

DOI: 10.1039/xxxxxxxxxx

www.rsc.org/journalname

Nanocarbon materials, including the sp^2 hybridized two-dimensional graphene and one-dimensional carbon nanotubes, and the sp^1 hybridized one-dimensional carbyne, are being considered for the next generation of integrated optoelectronic devices. The strong electron-phonon coupling present in these nanocarbon materials makes Raman spectroscopy an ideal tool to study and characterize material and device properties [1]. Near-field Raman spectroscopy combines non-destructive chemical, electrical, and structural specificity with nanoscale spatial resolution, making it an ideal tool for studying nanocarbon systems. Here we use near-field Raman spectroscopy to study strain, defects, and doping in different nanocarbon systems.

1 Introduction

Nanocarbon materials, such as carbon nanotubes and graphene, are being considered as a platform for next-generation integrated optoelectronics. Similar to semiconductor device technology, the electronic properties of nanocarbon materials can be engineered by introducing dopants and exploiting interfaces with other materials. For example, in semiconductors, electron concentration and electrical conductivity can be varied over six orders of magnitude by varying doping densities [2]. Furthermore, optical emission time constants and quantum efficiencies can be varied over four to five orders of magnitude by varying defect concentrations. Virtually every practical application of semiconductors relies on the effects of dopants, defects, and interfaces. Similarly, it can be expected that defects and dopants will have a strong influence on future nanocarbon devices. For example, graphene transitions from conducting to semiconducting when it is cut into a narrow ribbon, with a bandgap that depends on the ribbon width, the edge chirality, and the nature of the edges, demonstrating the strong influence of localized states on material transport properties. Any nanocarbon-based device engineering relies on a solid understanding of the electronic, structural, and optical properties of defects or dopants. The ability to zoom in on single defects and measure local physical properties is an important step in realizing these technologies.

A variety of high spatial resolution techniques have been applied for the systematic study of nanocarbon materials [3]. For example, transmission electron microscopy (TEM) has been used to determine nanotube structures [4] and low-temperature scanning tunneling microscopy (STM) has been applied to investigate the electronic density of states [5]. However, none of these techniques provides the ability to simultaneously probe the electronic, chemical, and structural properties of nanocarbons. Raman scattering, on the other hand, uses a non-destructive optical excitation to probe characteristic vibrational modes, which are directly linked to unique structural and electronic material properties [6–10]. However, the spatial resolution of Raman scattering is, traditionally, diffraction limited to roughly $\lambda/2$, λ being the wavelength of the exciting radiation, making it difficult to spatially isolate and investigate the effect of defects and dopants on the local material properties.

Here, we use near-field Raman scattering to study local features in different nanocarbon materials, including graphene, carbon nanotubes, and carbyne. Near-field Raman scattering, also referred to as tip-enhanced Raman scattering (TERS), is a spectroscopic technique that makes it possible to perform vibrational analysis with nanoscale spatial resolution, typically in the range of 10-20nm [11–13]. It uses a laser-irradiated metal tip acting as an optical antenna [14]. The antenna localizes and enhances the incident radiation at its apex, thereby serving as a highly-confined optical excitation source for Raman scattering (see Fig. 1). A near-field hyperspectral image of a sample is acquired by raster-scanning the sample below the tip and recording, pixel-by-pixel, a Raman scattering spectrum. The technique has been used to characterize local strain and structural defects in carbon nanotubes [15,16] and graphene [17], and to investigate the influence of the local environment on the optoelectronic properties [18–21]. We have extended the technique beyond

[a] Photonics Laboratory, ETH Zürich, 8093 Zürich, Switzerland.
[b] Material Measurement Laboratory, National Institute of Standards and Technology, Gaithersburg, MD, 20899, USA.
[c] Departamento de Física, Universidade Federal de Minas Gerais, Belo Horizonte, MG 30123-970, Brazil.
‡ www.photonics.ethz.ch

imaging to measure phonon correlation lengths in graphene samples[22]. Recently, TERS combined with STM has pushed optical spectroscopy to the sub-molecular level, demonstrating atomic-scale resolution[23].

This article is organized as follows: In Sec. 2 we introduce the experimental geometry and methodology used in our near-field studies of nanocarbon materials. Sections 3-5 introduce TERS findings of two-dimensional graphene (Sec. 3), one-dimensional carbon nanotubes (Sec. 4), and one-dimensional linear carbon chains (Sec. 5). Finally, we conclude by discussing the importance of TERS measurements and methodologies in the development of nanocarbon optoelectronic devices, in Sec. 6.

2 Experimental Techniques

Our near-field Raman experiments are performed with a home-built microscope[12,24], schematically shown in Fig. 1. The setup consists of a scanning probe microscope positioned on top of an inverted confocal microscope. First, a continuous-wave laser beam is converted to a radially polarized mode to ensure a strong longitudinal field component at the laser focus[25]. It is then sent into the inverted microscope where it is reflected by a dichroic beam-splitter and focused from below onto the sample surface by a high-numerical aperture objective. The scanning probe microscope is outfitted with an optical antenna as the probe. The antenna is positioned in the center of the optical focal spot and held in close proximity above the sample surface with a shear-force feedback system[26,27] with a force sensitivity of a few pico-Newtons. The laser-irradiated antenna (e.g. tip, pyramid, nanoparticle) localizes incident radiation to a subwavelength-sized spot, thereby generating a nanoscale excitation source for local Raman scattering with the sample surface. The locally scattered field is collected by the same objective lens, filtered by a combination of interference filters, and then detected by either a single photon-counting detector or a spectrograph equipped with a liquid nitrogen cooled CCD. The sample is mounted on a $40 \times 40\,\mu\text{m}^2$ closed-loop piezo scan-bed. Simultaneous optical and topographic images are formed by raster-scanning the sample in the horizontal plane between the objective and tip. The control electronics consist of a modified controller for STM. It is used for controlling the scan-bed, tip-sample separation, and image acquisition. The entire setup is placed inside a light-free, acoustically damped enclosure located on a floating optical table.

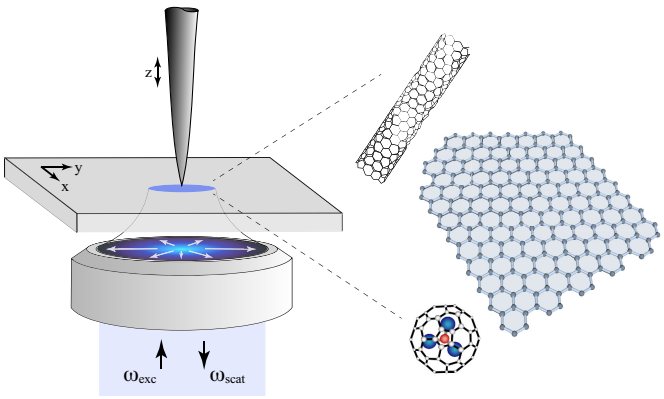

Fig. 1 Schematic diagram of the experimental setup. A radially polarized laser excitation is focused by a high-numerical aperture objective onto a sample from below. An optical antenna, attached to a piezo-electric tuning fork, is positioned into the center of the optical focus and is held in close proximity to the sample surface with shear-force feedback. Scattered optical signal is collected by the same objective, filtered by appropriate interference filters, and detected by either a single photon-counting detector or a spectrograph equipped with a liquid nitrogen cooled CCD. Simultaneous optical and topographic images are formed by raster-scanning the sample between the objective and tip.

We have demonstrated the applicability of a range of different optical antenna geometries for near-field microscopy including a sharp metallic wire[24,28], a single gold particle[29,30], cascaded gold particles[31], and highly reproducible pyramid optical antennas[32]. The pyramid antennas, due to their reproducibly high resolution and large field enhancements are the geometry we are currently using and will be briefly discussed. The pyramids are prepared by evaporating gold or silver onto a silicon template with inverted pyramidal pits, generally with a base of $20 \times 20\,\mu\text{m}^2$, generating metallic pyramid shells. Following a lift-off of the interstitially deposited metal, the end of a thin tungsten wire is attached to the inside of the pyramid shell using a standard two-part epoxy. The pyramid is then pulled out of the silicon template, exposing the outer region and the tip apex. A representative SEM image of a prepared pyramid antenna is shown in Fig. 2(a), where the tungsten wire extends downwards. As shown in Fig. 2(b), we determine the spatial resolution of the complete imaging apparatus based on single-molecule fluorescence images. A typical spatial imaging resolution for a pyramid antenna is $\sim 20\,\text{nm}$, and depends on the physical size of the tip apex. Additionally, the fluorescence enhancement of the tip, or relative detected signal intensity between a near-field excited molecule and far-field excited molecule, can be mapped by monitoring the single-molecule fluorescence intensity as a function of the tip-molecule separation. Typical fluorescence enhancement factors are on the order of 50–100-fold, corresponding to a localized electric field enhancement on the order of 10.

3 Graphene

Raman spectroscopy has been extensively applied to study the material properties of graphene such as defect density, carrier concentration, strain, and number of layers[33–39]. As such, TERS is an ideal technique for characterizing nanoscale graphene devices. Recently, the high spatial resolution and sensitivity of TERS has been used to measure Raman bands at edges and local strain in graphene[17,40,41]. Additionally, TERS has non-imaging applications where we have utilized the optical antenna as a nanometric, positionable, illumination source to measure the correlation length of optical phonons[22].

Being an sp^2 carbon system, the Raman spectrum of graphene has three primary features[1]. The most prominent band for single-

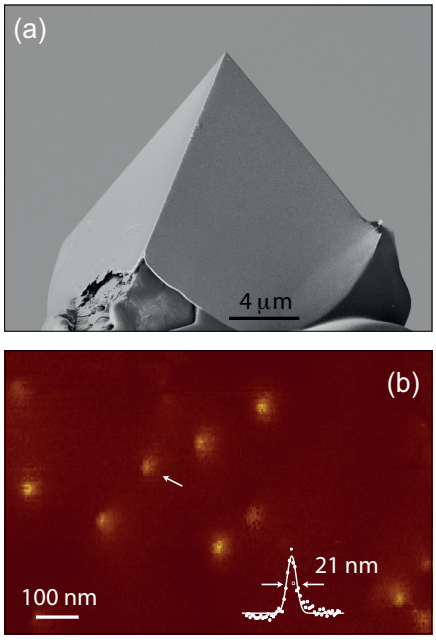

Fig. 2 The pyramid antenna and near-field resolution. (a) An SEM image of a gold pyramid tip. The base of the pyramid is $20 \times 20\,\mu m^2$ and tip apex is on the order of 10 nm. (b) A near-field single-molecule fluorescence image used to characterize the local field confinement of the pyramid antenna. The inset shows a cross section of the single-molecule marked with the white arrow. There is an imaging resolution of $\sim$21 nm.

layer graphene, known as the G′ or 2D band ($\sim 2700\,cm^{-1}$), belongs to the totally symmetric irreducible representation A_1' and is readily observable in all sp^2 carbon systems[1]. The G′ band is commonly used to determine the number of graphene layers. The second strongest band in pristine graphene is the double degenerate G band ($\sim 1600\,cm^{-1}$) with E_{2g} symmetry in the irreducible representation[38,42]. Both the G and G′ bands are present everywhere on a graphene flake and they are often used to characterize the strain and doping in the graphene flake[38]. The final primary feature is the disorder-induced D band ($\sim 1350\,cm^{-1}$) which has the same symmetry as the G′ band[38,42]. Unlike the G and G′ bands, the D band requires a lattice defect to be Raman active and is therefore highly localized to edges with armchair chirality in pristine graphene flakes[37,39,40,43,44].

The localized nature of the D band is determined by the phase-breaking length of carriers at optical energies ($\sim$1-3 eV), which is important for determining the carrier mobility in optoelectronic devices. The influence of edges is particularly important for the electronic properties of graphene nanoribbons[45]. Understanding and controlling the impact of defects on electronic properties is crucial for making further progress towards graphene based optoelectronic devices such as transparent displays and high-speed photodetectors.

Far-field and near-field Raman intensity images of the G′ band from a graphene flake are shown in Fig. 3(a,b), respectively. The color contrast in Fig. 3(a) is scaled by $\times$2 relative to Fig. 3(b). This data was acquired using a gold pyramid tip illuminated with a 632.8 nm laser. To further characterize the graphene flake, a near-field spectrum was acquired at the edge (square in Fig. 3(b)) and in the center (circle in Fig. 3(b)) of the flake, plotted in Fig. 3(c) in black and red, respectively. The Raman spectra indicate that the flake is single-layer and pristine since the D band is highly localized to the edge.

Fig. 4 shows a hyperspectral line-scan across the edge of another graphene flake. This data was acquired with a 632.8 nm laser and a silver pyramid tip. The sample was scanned below the illuminated tip and a complete Raman spectrum was acquired at each spatial location. The resulting colormap of the near-field Raman intensities is presented in Fig. 4(a), which illustrates that the G and G′ bands are continuous over the flake whereas the D band is highly localized at the edge (white arrow). The spectra were fit with single Lorentzians and the resulting amplitudes are plotted in Fig. 4(b,c). Fig. 4(b) shows that the D band is highly localized at the edge. The measured width is due to a convolution of the tip resolution with the D band spatial extent of $\sim$4 nm[37,40,43,44]. The G and G′ bands are shown in Fig. 4(c)

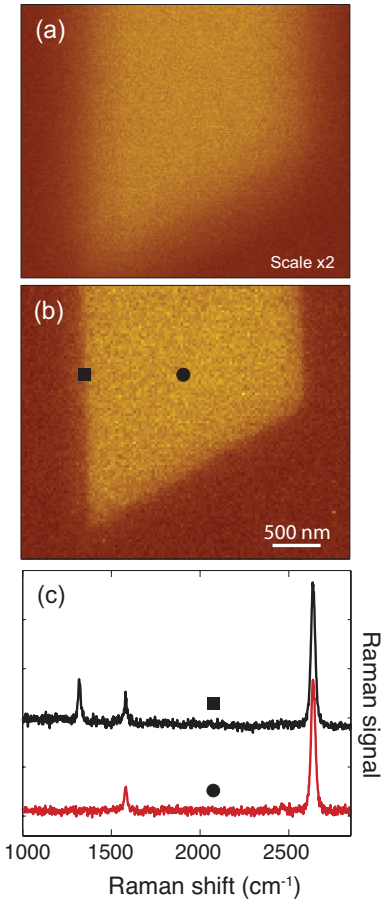

Fig. 3 Near-field Raman imaging of graphene. (a) Far-field and (b) near-field intensity images of the G′ band. The color contrast in (a) is scaled by $\times$2. (c) Near-field Raman spectra acquired at the edge (black) and center (red) of the flake as indicated by the square and circle in (b), respectively.

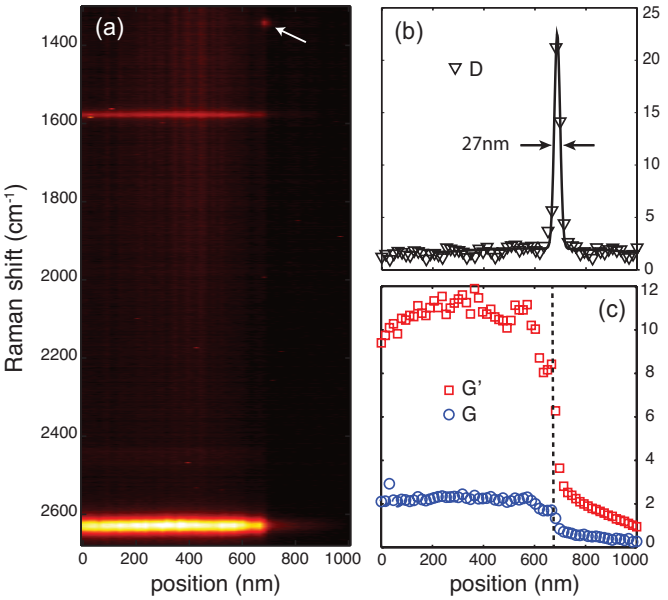

Fig. 4 Hyperspectral line-scan across a graphene flake edge. (a) Colormap of the near-field Raman intensities acquired by scanning the tip from the center of the flake (0 nm) across the edge (∼675 nm) and onto the glass substrate. The white arrow indicates the D band localized at the edge. (b), (c) Plots of the amplitude of the D (black triangles), G (blue circles), and G′ (red squares) bands.

as blue circles and red squares, respectively. The amplitudes of the G and G′ bands are continuous over the flake and sharply decrease as the tip transitions off the flake.

While these measurements were concerned with edges in pristine graphene, the demonstrated resolution and signal enhancement illustrates that TERS is capable of measuring single defects and local strains in a two-dimensional graphene device. Both of which will be necessary as graphene devices transition from academic demonstrations to industrial products.

4 Carbon Nanotubes

Carbon nanotubes are formed by rolling graphene into a tubular structure. As such, carbon nanotubes are still sp^2 systems and have Raman active modes that are similar to graphene. Single walled carbon nanotubes (SWNTs) present a combination of two properties that are ideal for near-field Raman experiments: (i) a strong Raman response (strong electron-phonon coupling combined with resonance matching in the optical absorption/emission), and (ii) a truly one dimensional character and nearly one-dimensional physical geometry that can be correlated with the optical response[1]. For this reason, carbon nanotubes are often chosen as prototypes for near-field Raman studies and were naturally involved in the early demonstration of the TERS effect[12]. In this section, we discuss how the innate applicability of the TERS effect on carbon nanotubes advanced the understanding of sp^2 nanocarbon photophysics.

Using near-field Raman scattering we are able to resolve localized features in the nanotube structure with a resolution of 10–20 nm. We have observed that the intensity of Raman lines along many nanotubes is non-uniform and we tentatively assigned this observation to defects in the different tube structures; however, it was suggested that the observation could be related to interactions of the tube with the supporting substrate. A series of experiments finally confirmed that the substrate has only a minor effect on the Raman lines[21] and that the observed localization of Raman modes was indeed due to nanotube inhomogeneities. The strongest support for these conclusions comes from measurements that were performed on nanotubes grown by different methods but using the same substrates. We found that some tubes are uniform over many tens of microns in length whereas other tubes show a high density of localized features. Generally, nanotubes grown by the chemical vapor deposition (CVD) method showed the lowest defect density. So-called serpentine nanotubes can be grown by using miscut quartz surfaces[46]; during CVD growth the nanotubes wind up in the form of serpentines, as shown in Fig. 5. The high quality of serpentine nanotubes allowed us to quantitatively study the mechanism of near-field Raman enhancement[13]. Our studies revealed that the near-field Raman intensity is inversely proportional to the 11^{th} power of the separation between the tip and the nanotube.

Analogous to graphene, the position and lineshape of Raman modes reveals much about the structure of the sp^2 carbon system. For example, the electronic properties of SWNTs strongly depend on the nanotube chirality, and Raman spectroscopy is one of the primary techniques used to probe the large variety of possibilities[1]. The tube chirality determines if the nanotube is metallic or semiconducting as well as the optical transition energies. Therefore, the structural characterization (chirality determination) of carbon nanotubes is extremely important for opotelectronic applications of carbon nanotubes. The chirality of the nanotube is determined by the radial breathing mode (RBM) frequency and resonance excitation profile[1].

The high resolution and sensitivity of TERS provides for the local characterization of SWNT junctions generated by abrupt chirality changes. First, the junction itself is a structural defect which can be detected by the presence of the disorder-induced

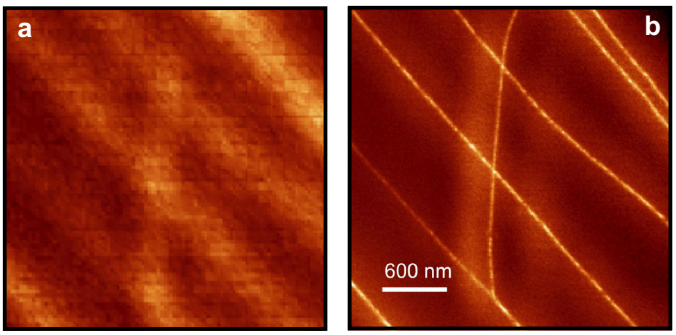

Fig. 5 (a) Confocal Raman image (G band intensity) of CVD grown SWNTs. (b) Corresponding near-field Raman image.

D band[47]. Second, changes in RBM frequency, which strongly depends on the tube diameter and consequently on the tube chirality, can be monitored. Third, the lineshape of the bond-stretching G band is different for metallic and semiconducting nanotubes. Combined, we have used TERS to provide spectroscopic evidence for the existence of local semiconducting-metal SWNT junctions[19].

Local semiconducting-metal transitions in SWNTs can also be induced by pressure[48,49]. This property was explored by Ref.[50], where the authors used TERS to measure the local Raman response of an X-shape crossing of two carbon nanotubes. By comparing the G band shape in the TERS spectra taken at the crossing point and far from it, the authors concluded that the upper tube suffered a semiconducting-metal transition due to a structural deformation (applied pressure) caused by the presence of the tube underneath. The effects of stresses on a nanotube were also explored in Ref.[51], where the authors applied controlled forces on an isolated semiconducting nanotube using the near-field probe itself. The authors observed local changes in the G band lineshape and intensity as a function of applied pressure on the nanotube, corresponding to the nanometric deformation of the nanotube itself. In Ref.[52], the same group used TERS to measure the effects of strain in SWNTs. The authors used an atomic force microscopy probe to apply lateral forces on isolated SWNTs. Again, TERS was used to extract detailed information regarding the induced mechanical deformations, and therefore the generated strain, by observing shifts in the G band frequency. Besides detecting mechanical distortions, near-field Raman spectroscopy is also very sensitive to local chemical environments, and a recent study has demonstrated chemical variations in SWNTs by TERS with $\sim 2\,\mathrm{nm}$ resolution[53].

Additionally, the effect of defects can be detected by spectral shifts in the Raman bands. Because electrons and phonons are strongly coupled in sp^2 carbon systems a defect can cause renormalization of electron and phonon energies. For defect-free and undoped SWNTs, the G′ band consists of a single peak centered at $\nu_{G'} = 2{,}676\,\mathrm{cm}^{-1}$ (for a 632.8 nm excitation). Upon doping, however, we observe that a new peak appears at lower/higher frequency for n/p doping. This new peak is slightly shifted from the main G′ peak and the shift is representative of an increase (decrease) in electron velocity near a negatively (positively) charged defect[16].

5 Carbyne

The newest allotrope to the carbon revolution is the one-dimensional carbyne. Carbyne is an infinite linear chain of carbon atoms which, unlike the other discussed carbon allotropes, is characterized by sp^1 hybridized bonds. Although it was proposed originally in the 1960s[54–57], its realization was subject to much controversy[58,59]. The first indisputable proof of linear carbon chains (LCCs) came from polyynes, or short LCCs that are stabilized by large end-capping groups[60]. Now, it has been demonstrated that carbon nanotubes can be utilized as both nanoreactors for the growth of LCCs and additionally serve to protect the chain from the ambient environment[61]. Using an optimized fabrication methodology, long linear carbon chains (LLCCs), consisting of thousands of carbon atoms, have been grown inside of double walled carbon nanotubes (DWCNTs, with the whole system referred to as LLCCs@DWCNTs)[62], that will be discussed here.

LCCs contained within carbon nanotubes are still a new system with potentially contradicting theoretical and experimental findings. Of primary concern for both Raman studies as well as applications in optoelectronics are Peierls distortions[63]. Theoretical studies have shown that there is a slight energetic preference for an LCC to have a polyynic (alternating single-triple bonds) conformation in free space, meaning that the chain is both semiconducting and Raman active; however, upon insertion into a nanotube, theoretical studies on the bond length alternation (BLA) vary, meaning that is unclear if LCCs@CNTs are, in general, metallic or semiconducting[64–66]. Despite these calculations, we find there to be a strong resonance Raman response for LLCCs@DWCNTs[62], although it is possible that there are additional, undetected, LCCs with zero BLA. This strong Raman response, combined with the well understood nanotube Raman response, makes Raman spectroscopy an ideal tool to study the physical and electrical properties of the combined system.

Theoretical calculations have reproduced the Raman shifts observed in studies of chemically synthesized polyynes of known size, showing that longer chains have a lower-energy Raman shift[67]. Thus far, far-field ensemble measurements have been used to characterize the Raman response of the LLCCs@DWCNTs and have supported this theory; however, ensemble averaging combined with low spatial resolution has made it impossible to directly measure individual chain lengths and corresponding spectra[62]. Shown in Fig. 6, we have used TERS to resolve individual LLCCs that are hosted inside a single DWCNT.

Near-field hyperspectral imaging has revealed a complex local interaction between the LLCCs and the enclosing DWCNT. Fig. 6(a) shows the superposition of a near-field Raman image (color) of an isolated DWCNT containing multiple LLCCs and its corresponding topographic image (grayscale). We are able to measure the physical length of the individual chains (200 – 800 nm) and correlate it with the respective Raman shifts ($1804 - 1786\,\mathrm{cm}^{-1}$) across a variety of samples. A near-field hyperspectral image allows us to simultaneously visualize the Raman response of the LLCC and the DWCNT. The spectra shown in Fig. 6(b), corresponding to positions just to the left of the diamond, circle, and square in Fig. 6(a), are all normalized to the intensity of the LLCC mode at $\sim 1800\,\mathrm{cm}^{-1}$ in the bottom spectrum and are offset from each other for visibility. Depending on the sampling location relative to the location of the LLCC, the relative ratios between the outer nanotube RBM at $\sim 204\,\mathrm{cm}^{-1}$, the inner nanotube RBM at $\sim 362\,\mathrm{cm}^{-1}$, and the G band at $\sim 1590\,\mathrm{cm}^{-1}$ vary greatly, while the D band component at $\sim 1315\,\mathrm{cm}^{-1}$ is rather constant. Studies of LCCs in nanotubes

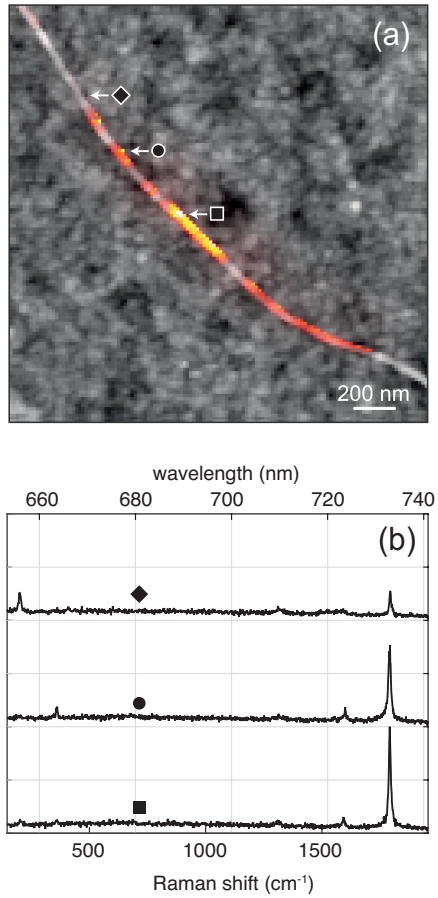

Fig. 6 Near-field Raman imaging of long linear carbon chains (LLCCs) in double walled carbon nanotubes. (a) A superposition of the near-field LLCC mode image (color) acquired with a narrow band-pass filter centered at 735 nm and the corresponding topographic image (grayscale). (b) Near-field spectra of the nanotube just to the left of the positions marked in (a) with the diamond, circle, and square. All spectra are normalized to the LLCC mode at $\sim 1800\,cm^{-1}$ in the bottom spectrum and are offset from each other by 1 for visibility. A complex interplay between the relative intensities of the outer nanotube RBM at $\sim 204\,cm^{-1}$, the inner nanotube RBM at $\sim 362\,cm^{-1}$, and the G band at $\sim 1590\,cm^{-1}$, relative to the LLCC mode, is observed.

have both predicted[68,69] and measured[70] shifts in the RBM upon filling, while other studies have noticed a dramatic decrease in the RBM of a Mo-filled nanotube[71]. This complex interaction has not been observed in ensemble measurements and highlights the need for the resolution and sensitivity afforded by near-field spectroscopy.

6 Conclusions and Outlook

The tunable optoelectric properties of nanocarbon materials makes them ideal for the next generation of optoelectronic devices. Combined with other near-field microscopy techniques, TERS allows for a deep understanding of the physical processes taking place. Current optoelectronic studies of carbon nanotubes highlights the synergy between Raman, photoluminescence (PL) and electroluminescence (EL) microscopy and their importance for real device engineering.

Several works have explored near-field PL as a probe for local changes in carbon nanotubes[18,20,72–75]. Our work of combined Raman and near-field PL measurements of carbon nanotubes revealed the localized nature of PL emission from defects[18], which may have implications both for nanocarbon-based light-emission and photo-detection. Additionally, TERS has been combined with near-field EL microscopy to study carbon nanotube device junctions[76]. TERS was used to localize a Schottky junction between at least one metallic and one semiconducting nanotube, and confirm that the EL emission originated from the junction. This work further proved the reciprocity theorem, which states that optical antennas are not only able to increase the efficiency of optical absorption, but also optical emission[77]. We have also characterized graphene EL from STM experiments[78] and applied this knowledge to fabricate and characterize an antenna-coupled graphene photodetector[79].

While the study of sp^2 nanocarbons is still under development, the study of carbyne is only in its infancy. Even still, TERS has already demonstrated the ability to locally sample the complex interaction between overlapping sp^1 and sp^2 orbitals that will be essential to facilitate devices based on this novel material. The chemical sensitivity and non-destructive nature of Raman spectroscopy, combined with the high-spatial resolution and topographic information afforded by near-field microscopy, makes TERS ideal to study nanocarbons.

7 Acknowledgements

This work was funded by the Swiss National Science Foundation (SNF) under the NCCR-QSIT program and grant CR2212_152944. LGC acknowledges FAPEMIG and CNPq. We thank Ernesto Joselevich for the serpentine nanotube samples, Thomas Pichler, Lei Shi, and Philip Rohringer for the carbyne samples, Sang-Hyun Oh and Tim Johnson for template stripped gold pyramids, and Ado Jorio for valuable discussions.

References

1 A. Jorio, G. Dresselhaus and M. S. Dresselhaus, *Carbon Nanotubes: Advanced Topics in the Synthesis, Structure, Properties and Applications*, Springer, Berlin, 2008, vol. 111.
2 J. Singh, *Physics of Semiconductors and Their Heterostructures*, McGraw-Hill, 1993.
3 *Carbon Nanotubes*, ed. M. S. Dresselhaus, G. Dresselhaus and P. Avouris, Springer, Berlin, 2001, vol. 80.
4 L.-C. Qin, X. Zhao, K. Hirahara, Y. Miyamoto, Y. Ando and S. Iijima, *Nature*, 2000, **408**, 50.
5 T. W. Odom, J.-L. Huang, P. Kim and C. M. Lieber, *Nature*, 1998, **391**, 62–64.
6 A. Jorio, R. Saito, J. H. Hafner, C. M. Lieber, M. Hunter, T. Mc-

Clure, G. Dresselhaus and M. S. Dresselhaus, *Phys. Rev. Lett.*, 2001, **86**, 1118.
7 Z. Yu and L. Brus, *J. Phys. Chem. B*, 2001, **105**, 1123–1134.
8 A. Mews, F. Koberling, T. Basché, G. Philipp, G. S. Duesberg, S.Roth and M. Burghard, *Advanced Materials*, 2000, **12**, 1210.
9 J. Maultzsch, S. Reich, C. Thomsen, S. Webster, R. Czerw, D. L. Carroll, S. Vieira, P. Birkett and C. Rego, *Appl. Phys. Lett.*, 2002, **81**, 2647.
10 G. S. Duesberg, I. Loa, M. Burghard, K. Syassen and S. Roth, *Phys. Rev. Lett.*, 2000, **85**, 5436–5439.
11 R. M. Stöckle, Y. D. Suh, V. Deckert and R. Zenobi, *Chem. Phys. Lett.*, 2000, **318**, 131–136.
12 A. Hartschuh, E. Sanchez, X. Xie and L. Novotny, *Phys. Rev. Lett.*, 2003, **90**, 095503.
13 L. G. Cançado, A. Jorio, A. Ismach, E. Joselevich, A. Hartschuh and L. Novotny, *Phys. Rev. Lett.*, 2009, **103**, 186101.
14 L. Novotny and S. J. Stranick, *Ann. Rev. Phys. Chem.*, 2006, **57**, 303–331.
15 N. Anderson, A. Hartschuh and L. Novotny, *Materials Today*, May 2005, **8**, 50–54.
16 I. O. Maciel, N. Anderson, M. A. Pimenta, A. Hartschuh, H. Qian, M. Terrones, H. Terrones, J. Campos-Delgado, A. M. Rao, L. Novotny and A. Jorio, *Nature Mat.*, 2008, **7**, 878 – 883.
17 R. Beams, L. G. Cancado, A. Jorio, A. N. Vamivakas and L. Novotny, *Nanotechnology.*, 2015, **26**, 175702.
18 A. Hartschuh, H. Qian, A. J. Meixner, N. Anderson and L. Novotny, *Nano Lett.*, 2005, **5**, 2310.
19 N. Anderson, A. Hartschuh and L. Novotny, *Nano Lett.*, 2007, **7**, 577–582.
20 H. Qian, C. Georgi, N. Anderson, A. A. Green, M. C. Hersam, L. Novotny and A. Hartschuh, *Phys. Stat. Sol. B*, 2008, **245**, 2243–2246.
21 J. Soares, A. P. Barboza, D. Nakabayashi, P. Araujo, N. B. Neto, N. Shadmi, T. Yarde, A. Ismach, N. Geblinger, E. Joselevich, C. Vilani, L. G. Cancado, L. Novotny, G. Dresselhaus, M. Dresselhaus, B. Neves and M. Mazzoni, *Nano Lett.*, 2011, **10**, 5043–5048.
22 R. Beams, L. G. Cancado, S.-H. Oh, A. Jorio and L. Novotny, *Physical Review Letters*, 2014, **113**, 186101.
23 R. Zhang, Y. Zhang, Z. Dong, S. Jiang, C. Zhang, L. Chen, L. Zhang, Y. Liao, J. Aizpurua, Y. Luo *et al.*, *Nature*, 2013, **498**, 82–86.
24 L. G. Cançado, A. Hartschuh and L. Novotny, *J. Raman Spectrosc.*, 2009, **40**, 1420–1426.
25 L. Novotny, M. R. Beversluis, K. S. Youngworth and T. G. Brown, *Phys. Rev. Lett.*, 2001, **86**, 5251.
26 K. Karrai and R. D. Grober, *Appl. Phys. Lett.*, 1995, **66**, 1842–1844.
27 T. R. Albrecht, P. Grütter, D. Horne and D. Rugar, *J. Appl. Phys.*, 1991, **69**, 668.
28 L. Novotny, E. J. Sanchez and X. S. Xie, *Optics & Photonics News*, 1999, **10**, 24.
29 P. Anger, P. Bharadwaj and L. Novotny, *Phys. Rev. Lett.*, 2006, **96**, 113002.
30 P. Bharadwaj, R. Beams and L. Novotny, *Chem. Science*, 2011, **2**, 136–140.
31 C. Höppener, Z. Lapin, P. Bharadwaj and L. Novotny, *Phys. Rev. Lett.*, 2012, **109**, 017402.
32 T. W. Johnson, Z. J. Lapin, R. Beams, N. C. Lindquist, S. G. Rodrigo, L. Novotny and S.-H. Oh, *ACS Nano*, 2012, **6**, 9168–9174.
33 L. G. Cançado, M. A. Pimenta, B. R. A. Neves, M. S. S. Dantas and A. Jorio, *Phys. Rev. Lett.*, 2004, **93**, 247401.
34 A. C. Ferrari, J. C. Meyer, V. Scardaci, C. Casiraghi, M. Lazzeri, F. Mauri, S. Piscanec, D. Jiang, K. S. Novoselov, S. Roth and A. K. Geim, *Phys. Rev. Lett.*, 2006, **97**, 187401.
35 A. Das, S. Pisana, B. Chakraborty, S. Piscanec, S. K. Saha, U. V. Waghmare, K. S. Novoselov, H. R. Krishnamurthy, A. K. Geim, A. C. Ferrari and A. K. Sood, *Nature Nanotech.*, 2008, **3**, 210.
36 T. M. G. Mohiuddin, A. Lombardo, R. R. Nair, A. Bonetti, G. Savini, R. Jalil, N. Bonini, D. M. Basko, C. Galiotis, N. Marzari, K. S. Novoselov, A. K. Geim and A. C. Ferrari, *Physical Review B*, 2009, **79**, 205433.
37 M. M. Lucchese, F. Stavale, E. H. Martins Ferreira, C. Vilahn, M. V. O. Moutinho, R. B. Capaz, C. A. Achete and A. Jorio, *Carbon*, 2010, **48**, 1592–1597.
38 A. C. Ferrari and D. M. Basko, *Nature Nanotech.*, 2013, **8**, 235–246.
39 R. Beams, L. G. Cançado and L. Novotny, *Journal of Physics: Condensed Matter*, 2015, **27**, 083002.
40 W. Su and D. Roy, *J. Vac. Sci. and Technol. B*, 2013, **31**, 041808.
41 L. G. Cancado, R. Beams, A. Jorio and L. Novotny, *Physical Review X*, 2014, **4**, 031054.
42 A. Jorio, M. S. Dresselhaus, R. Saito and G. Dresselhaus, *Raman Spectroscopy in Graphene Related System*, Wiley-VCH, Weinheim, Germany, 1st edn, 2011.
43 C. Casiraghi, A. Hartschuh, H. Qian, S. Piscanec, C. Georgi, A. Fasoli, K. S. Novoselov, D. M. Basko and A. C.Ferrari, *Nano Lett.*, 2009, **9**, 1433–1441.
44 R. Beams, L. G. Cancado and L. Novotny, *Nano Lett.*, 2011, **11**, 1177–1181.
45 K. A. Ritter and J. W. Lyding, *Nature Materials*, 2009, **8**, 235–242.
46 N. Geblinger, A. Ismach and E. Joselevich, *Nature Nanotech.*, 2008, **3**, 195.
47 C. Georgi and A. Hartschuh, *Applied Physics Letters*, 2010, **97**, 143117.
48 B. Shan, G. W. Lakatos, S. Peng and K. Cho, *Applied Physics Letters*, 2005, **87**, –.
49 L. Vitali, M. Burghard, P. Wahl, M. A. Schneider and K. Kern, *Phys. Rev. Lett.*, 2006, **96**, 086804.
50 Y. Okuno, Y. Saito, S. Kawata and P. Verma, *Physical review letters*, 2013, **111**, 216101.
51 T.-a. Yano, P. Verma, Y. Saito, T. Ichimura and S. Kawata, *Nature Photonics*, 2009, **3**, 473–477.
52 T.-a. Yano, T. Ichimura, S. Kuwahara, F. HDhili, K. Uetsuki,

Y. Okuno, P. Verma and S. Kawata, *Nature Communications*, 2013, **4**, 2592.
53 C. Chen, N. Hayazawa and S. Kawata, *Nature Communications*, 2014, **5**, 2592.
54 V. I. Kasatochkin, A. M. Sladkov, Y. P. Kudryavtsev, N. M. Popov and V. V. Korshak, *Dokl. Akad. Nauk SSSR+*, 1967, **177**, 358–360.
55 A. E. Goresy and G. Donnay, *Science (New York, N.Y.)*, 1968, **161**, 363–4.
56 A. G. Whittaker and P. L. Kintner, *Science (New York, N.Y.)*, 1969, **165**, 589–91.
57 A. Sladkov and Y. Kudryavtsev, *Priroda*, 1969, **5**, 37–44.
58 P. P. Smith and P. R. Buseck, *Science*, 1981, **212**, 322–4.
59 P. P. Smith and P. R. Buseck, *Science*, 1982, **216**, 984–6.
60 W. A. Chalifoux and R. R. Tykwinski, *Comptes Rendus Chimie*, 2009, **12**, 341–358.
61 X. Zhao, Y. Ando, Y. Liu, M. Jinno and T. Suzuki, *Physical Review Letters*, 2003, **90**, 187401.
62 L. Shi, *PhD thesis*, Universität Wien, 2015.
63 R. E. Peierls, *Quantum theory of solids*, Clarendon, 1955.
64 A. Rusznyak, V. Zolyomi, J. Kurti, S. Yang and M. Kertesz, *Physical Review B*, 2005, **72**, 155420.
65 X. Fan, L. Liu, J. Lin, Z. Shen and J.-L. Kuo, *ACS Nano*, 2009, **3**, 3788–3794.
66 A. Tapia, L. Aguilera, C. Cab, R. Medina-Esquivel, R. de Coss and G. Canto, *Carbon*, 2010, **48**, 4057–4062.
67 S. Yang, M. Kertesz, V. Zolyomi and J. Kurti, *The Journal of Physical Chemistry A*, 2007, **111**, 2434–2441.
68 Z. L. Hu, X. M. Guo and C. Q. Ru, *Nanotechnology*, 2007, **18**, 485712.
69 Y. Liu, R. O. Jones, X. Zhao and Y. Ando, *Physical Review B*, 2003, **68**, 125413.
70 M. Jinno, Y. Ando, S. Bandow, J. Fan, M. Yudasaka and S. Iijima, *Chemical Physics Letters*, 2006, **418**, 109–114.
71 H. Muramatsu, T. Hayashi, Y. A. Kim, D. Shimamoto, M. Endo, M. Terrones and M. S. Dresselhaus, *Nano Letters*, 2008, **8**, 237–240.
72 H. Qian, T. Gokus, N. Anderson, L. Novotny, A. J. Meixner and A. Hartschuh, *Phys. Stat. Sol. B*, 2006, **243**, 1–5.
73 H. Qian, C. Georgi, N. Anderson, A. A. Green, M. C. Hersam, L. Novotny and A. Hartschuh, *Nano Lett.*, 2008, **8**, 1363–1367.
74 H. Qian, P. T. Araujo, C. Georgi, T. Gokus, N. Hartmann, A. A. Green, A. Jorio, M. C. Hersam, L. Novotny and A. Hartschuh, *Nano Lett.*, 2008, **8**, 2706–2711.
75 C. Georgi, M. Boehmler, H. Qian, L. Novotny and A. Hartschuh, *Phys. Stat. Sol. B*, 2009, **246**, 2683–2688.
76 N. Mauser, N. Hartmann, M. S. Hofmann, J. Janik, A. Hošgele and A. Hartschuh, *Nano letters*, 2014, **14**, 3773–3778.
77 P. Bharadwaj, B. Deutsch and L. Novotny, *Adv. Opt. Phot.*, 2009, **1**, 438 – 483.
78 R. Beams, P. Bharadwaj and L. Novotny, *Nanotechnology*, 2014, **25**, 055206.
79 C. Chakraborty, R. Beams, K. M. Goodfellow, G. W. Wicks, L. Novotny and N. A. Vamivakas, *Applied Physics Letters*, 2014, **105**, 241114.